

## Nonlinear Low-Fidelity Numerical Model of the Flared Folding Wingtip

Carrillo Córcoles, X.; De Breuker, R.; Sodja, J.

**DOI**

[10.2514/6.2023-0378](https://doi.org/10.2514/6.2023-0378)

**Publication date**

2023

**Document Version**

Final published version

**Published in**

AIAA SciTech Forum 2023

**Citation (APA)**

Carrillo Córcoles, X., De Breuker, R., & Sodja, J. (2023). Nonlinear Low-Fidelity Numerical Model of the Flared Folding Wingtip. In *AIAA SciTech Forum 2023* Article AIAA 2023-0378  
<https://doi.org/10.2514/6.2023-0378>

**Important note**

To cite this publication, please use the final published version (if applicable).  
Please check the document version above.

**Copyright**

Other than for strictly personal use, it is not permitted to download, forward or distribute the text or part of it, without the consent of the author(s) and/or copyright holder(s), unless the work is under an open content license such as Creative Commons.

**Takedown policy**

Please contact us and provide details if you believe this document breaches copyrights.  
We will remove access to the work immediately and investigate your claim.

# Nonlinear Low-Fidelity Numerical Model of the Flared Folding Wingtip

Xavier Carrillo Córcoles\*, Roeland De Breuker<sup>†</sup> and Jurij Sodja<sup>‡</sup>

Previous numerical and experimental studies have shown the load alleviation capabilities of the flared folding wingtip. However, they have also shown the complex dynamics of the system and the limitations in the results obtained by modeling such an aeroelastic system using linear models, which cannot capture the effects of the large wingtip deflections. Therefore, the current study presents a nonlinear time domain flexible multibody model comprising a linear beam representing the main wing, and a rigid body representing the wingtip and its nonlinear effects. In addition, the time domain model allows the simulation of the hinge release based on the load threshold, which was also studied experimentally. The structural model is coupled to quasi-steady aerodynamics strip theory to model the aerodynamic loads. The aerodynamic model is refined using the experimental steady-state results from the previous work and then compared to the experimental gust response from the same study. The model presents good agreement with the experimental results in the case of low and moderate-frequency gusts. However, the agreement is worse for high-frequency gusts as expected due to the assumption of quasi-steady aerodynamics. Furthermore, the model captures the same trends observed in the experiment for the hinge release load threshold. Finally, the time-marching model is also used to assess the nonlinear stability boundaries and the occurrence of limit cycle oscillations.

## Nomenclature

### Variables

$\mathbf{A}$	= state-space system matrix,
$a$	= non-dimensional distance from the semi-chord to the elastic axis,
$\underline{B}$	= state-space input vector,
$B_{fwt}$	= distance from the hinge to the tip of the FFWT, m
$B_h$	= distance from root to the hinge, m
$B_{lim}$	= distance from root to start of wind tunnel section, m
$B_{tot}$	= wing semispan, m
$b$	= semi-chord, m
$\mathbf{C}, \mathbf{K}, \mathbf{M},$	= damping, stiffness and mass matrices,
$\overline{\mathbf{C}}, \overline{\mathbf{K}}, \overline{\mathbf{M}},$	= generalised damping, stiffness and mass matrices,
$c$	= chord, m
$c_B$	= bending moment coefficient, $M_B / \frac{1}{2} \rho S B_{tot} U^2$
$E$	= kinetic energy, J
$F_h$	= total vertical force produced by the wingtip, N
$f_i, f_s, f_e$	= total, sectional and elliptic aerodynamic scaling factors
$h$	= vertical displacement degree of freedom, m

---

\*Researcher, Faculty of Aerospace Engineering, Aerospace Structures and Computational Mechanics, Kluyverweg 1 2629 HS Delft, X.CarrilloCorcoles@tudelft.nl

<sup>†</sup>Associate Professor, Faculty of Aerospace Engineering, Aerospace Structures and Computational Mechanics, Kluyverweg 1 2629 HS Delft, R.deBreuker@tudelft.nl, AIAA Associate Fellow

<sup>‡</sup>Senior scientist, Faculty of Aerospace Engineering, Aerospace Structures and Computational Mechanics, Kluyverweg 1 2629 HS Delft, J.Sodja@tudelft.nl, AIAA Senior Member

$\mathbf{I}$	= inertia tensor,
$k$	= reduced frequency, $k = \omega b/U$
$l_i, l_c, l_{nc}$	= local, circulatory and non circulatory sectional lift, N/m
$l_{fwt}$	= wingtip sectional lift, N/m
$M_\eta$	= total torsional moment produced by the wingtip, Nm
$M_\theta$	= total hinge moment produced by the wingtip, Nm
$m_{a,i}, m_{a,c}, m_{a,nc}$	= local, circulatory and non circulatory sectional aerodynamic moment, N
$m_{a,fwt}$	= wingtip sectional aerodynamic moment, N
$m_{fwt}$	= wingtip mass, kg
$N_{DOF}$	= number of degrees of freedom,
$N_{el}$	= number of elements,
$N_{fwt}$	= number of aerodynamic nodes of the wingtip,
$N_{nd}$	= number of nodes on the main wing,
$\underline{q}$	= external loads vector,
$\underline{U}$	= airspeed, m/s
$U_g$	= gust airspeed, m/s
$V$	= potential energy, J
$\underline{v}_f$	= local airspeed vector at the wingtip, m/s
$\underline{R}_n(\mu)$	= rotation matrix of angle $\mu$ around axis $n$ ,
$t$	= time, s
$\alpha$	= angle of attack, $^\circ$
$\alpha_0$	= root angle of attack, $^\circ$
$\alpha_g$	= wingtip geometrical angle of attack, $^\circ$
$\beta$	= bending slope, $dh/dy$
$\gamma$	= total hinge angle, $\theta + \beta_t$ , $^\circ$
$\delta$	= numerical convergence constant,
$\varepsilon$	= steady-state square root of the square error, $\sqrt{(\underline{\psi} - \underline{\psi}_0)^T (\underline{\psi} - \underline{\psi}_0)}$
$\underline{\zeta}$	= vector of beam degrees of freedom $\{\dots\eta_i, h_i, \beta_i, \dots\}$ for $i = 1, 2, \dots, N_{nd}$
$\underline{\eta}$	= torsional angle, $^\circ$
$\underline{\eta}$	= vector of torsional degrees of freedom $\{\eta_1, \eta_2, \dots, \eta_{N_{nd}}\}$
$\underline{\theta}$	= fold angle, $^\circ$
$\Lambda$	= flare angle, $^\circ$
$\underline{\lambda}$	= vector of eigenvalues, $\lambda_i = a_i \pm ib_i$
$\xi$	= damping ratio, $a_i/\sqrt{a_i^2 + b_i^2}$
$\rho$	= air density, kg/m <sup>3</sup>
$\Phi$	= matrix of column eigenvectors,
$\underline{\chi}$	= vector of bending degrees of freedom $\{\dots, h_i, \beta_i, \dots\}$ for $i = 1, 2, \dots, N_{nd}$
$\underline{\psi}$	= vector of total degrees of freedom $\{\dots\eta_i, h_i, \beta_i, \dots, \theta\}$ for $i = 1, 2, \dots, N_{nd}$
$\underline{\underline{\Omega}}_{fwt}$	= wingtip rotational velocity vector, rad/s
$\omega$	= natural frequency, rad/s

## List of abbreviations

CG	= Center of Gravity
DLM	= Doublet Lattice Method
DOF	= Degree of Freedom
EOM	= Equation of Motion
FEM	= Finite Element Model
FFWT	= Flared Folding Wingtip
GLA	= Gust Load Alleviation
GVT	= Ground Vibration Test
LACA	= Linearised About Coast Angle

LCO	=	Limit Cycle Oscillations
RMS	=	Root Mean Square
TVLA	=	Time-Varying Linear Approximation
WRBM	=	Wing Root Bending Moment

## I. Introduction

AIRCRAFT aerodynamic efficiency can be improved by increasing the wingspan and thereby the aspect ratio of the main wing. However, increasing the wingspan can lead to an increased structural weight of the wing due to increased structural loads in the inboard section of the wing, reduced handling qualities due to reduced roll rate, and operational difficulties due to limited parking space at the airports [1].

To address the operational difficulties, Boeing [2] implemented a folding wingtip on the 777X, which can be folded when the airplane is on the ground and deployed before take-off. On the other hand, Wilson et al. [3] proposed a flared folding wingtip (FFWT) using a hinge at a flare angle, allowing the wingtip to rotate when released in flight to alleviate dynamic loads, such as gust loads, and to address the reduced maneuverability due to the span increase of the wing, in addition to increasing the aerodynamic efficiency.

The numerical analyses presented by Castrichini et al. [4] showed that the FFWT can reduce the wing root bending moment (WRBM) and provide means for gust load alleviation (GLA). These results were confirmed in wind tunnel tests. Cheung et al. [5, 6] showed the potential for passive load alleviation of the system, achieving peak load reductions between 30% and 60%, and studied the active control of the FFWT, which, depending on the phase of the actuation with respect to the gusts, can improve the GLA performance up to 80% reduction of the peak loads. In addition, the effect of the phase of the gust is also important when releasing the hinge, since the release instant affects the magnitude of the load alleviation, as reported by Castrichini et al. [7, 8].

Regarding the handling qualities, first Dussart et al. [9] in numerical analyses and later Healy et al. [10] in wind tunnel tests, found that it is possible to alleviate the reduction of steady roll rates caused by the wingspan increment when the FFWT is released. It is possible to recover between 60% and 80% of the roll rate of a wing without the wingtip extension.

To validate these findings in flight, Wilson et al. [11] used a scaled aircraft model based on the Airbus A321, the AlbatrossONE, that includes a hinge mechanism to lock and release the FFWT. The results confirmed the potential of the concept for load alleviation, with load reductions between 20% and 40% depending on the FFWT span, and presented the proof-of-concept with a gate-to-gate demonstration [12].

In continuation of their work, an aeroelastic experimental investigation was proposed to characterize how the load alleviation capabilities of the FFWT are affected by the variation of the wing stiffness, passive load alleviation using composite tailoring, and the variation of load threshold for releasing the hinge [13]. The wing model used in this study was designed using a linear numerical model relying on the doublet lattice method (DLM) to model the aerodynamics and a linear finite element model (FEM) to model the structure of the wing and FFWT. An elastic element with low torsional stiffness was used to model the free rotational degree of freedom of the hinge. However, it was not possible to release the hinge during the gust and the model did not account for the effect of the large rotations on the mass matrix and the aerodynamic loads. For this reason, during the experiment, it was found that the flutter speed was considerably lower than predicted (25% lower for the most flexible wing), leading to an onset of stable limit cycle oscillations (LCO), showing the limitations of the linear model.

Therefore, this study proposes a low-fidelity nonlinear aeroelastic model in the time domain to capture the complex behavior of the FFWT and improve the agreement of the numerical model with the experimental results. On the one hand, the proposed structural model is based on multi-body dynamics, connecting the main wing flexible body represented as a linear FE beam and a rigid body representing the FFWT and constrained by the kinematics of the flared hinge. On the other hand, the aerodynamic loads are modeled using strip theory, which simplifies the application of the loads on the structural elements and requires low evaluation times. In addition, such a model will allow the seamless inclusion of control surfaces without major modifications to extend it into an aeroservoelastic model suitable for conducting load alleviation studies considering both the FFWT and conventional control surfaces.

To conclude this introduction, the content of this paper is structured as follows. First, the numerical model will be described, starting with the derivation of the structural and aerodynamic models and continuing

with the assembly of the final nonlinear aeroelastic model. Next, the results of this model will be presented and compared to the experimental results from the previous work [13]. Finally, the conclusions of this study and the considerations for future work will be discussed.

## II. Numerical Model

The experimental work conducted on the FFWT relied on a linear numerical model to design the wind tunnel model. However, the results showed that the numerical model could not predict the flutter speed accurately. For this reason, this study presents a nonlinear model to improve the numerical predictions. In this section, the numerical model used in the aeroelastic analysis is presented. The Euler-Lagrange equations are used to derive the equations of motion (EOM). Therefore, the kinetic and potential energy expressions are developed for both the main wing and the FFWT. Afterward, the expressions for the external loads, the aerodynamic loads, are developed and introduced in the EOM to assemble the aeroelastic model. Finally, the corresponding nonlinear state-space system is used to assess the different conditions that were studied experimentally.

### A. Structural Model

The wing is divided into two bodies: the main wing is represented as a beam while the FFWT is represented as a rigid body lumped into a mass point with its corresponding moment of inertia tensor. These bodies are then connected using kinematic constraints that define the relative motion of the FFWT with respect to the tip of the main wing. In addition, a torsional spring is included at the hinge to represent the locking mechanism.

An overview of the wing model is presented in Figure 1, where  $\Lambda$  and  $\theta$  are the flare angle and fold angle respectively,  $B_{lim}$  is the distance from the root to the point where the wing is submerged in the flow,  $B_h$  is the distance from the root to the hinge,  $B_{fwt}$  is the length of the FFWT, and  $B_{tot}$  is the wing semi-span.

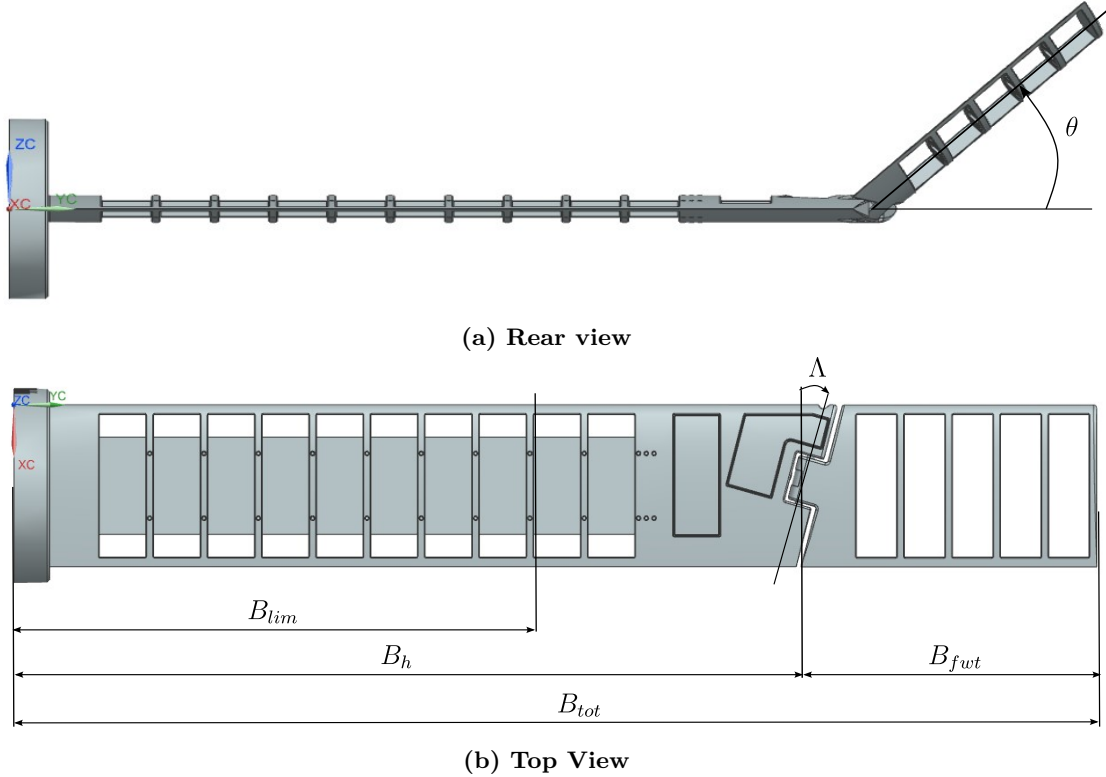


**Fig. 1** CAD representation of the wind tunnel model featuring a FFWT used in previous work [13].

### 1. Main Wing: Beam Model

The main wing is modeled using a finite element discretization of  $N_{el}$  elements, with two nodes per element, as presented by Hodges [14]. The wing is defined as an Euler-Bernoulli beam with three degrees of freedom (DOF) per node: the torsional angle,  $\eta$ , the vertical displacement,  $h$ , and the bending slope,  $\beta = \partial h / \partial y$ , as defined in Figure 2. The potential energy of the beam can be expressed as a sum of bending and torsional energy,  $V_b$  and  $V_\eta$  respectively, as expressed in matrix form in Equation 1, where  $\mathbf{K}_\eta$  and  $\mathbf{K}_b$  are the torsional and bending stiffness matrices, and  $\underline{\eta}$  and  $\underline{\chi}$  are the vectors with the respective degrees of freedom.

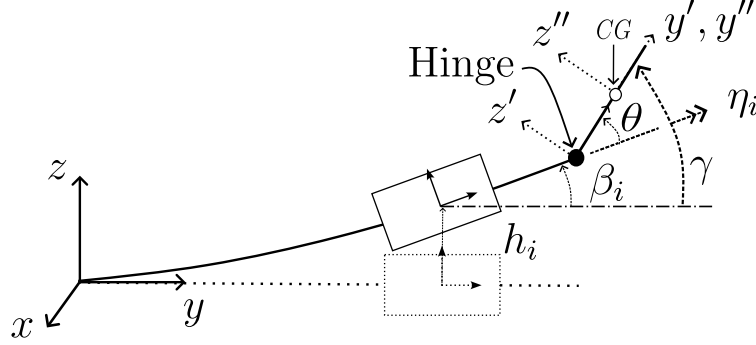


**Fig. 2** Schematic showing the reference system used for the beam elements and the moving reference systems,  $x'y'z'$  and  $x''y''z''$ .

$$V_\eta = \frac{1}{2} \underline{\eta}^T \mathbf{K}_\eta \underline{\eta} \quad V_b = \frac{1}{2} \underline{\chi}^T \mathbf{K}_b \underline{\chi} \quad (1)$$

Similarly, the kinetic energies,  $E_\eta$  and  $E_b$ , can be expressed in matrix form as presented Equation 2 using the mass matrices,  $\mathbf{M}_\eta$  and  $\mathbf{M}_b$ , and the time derivatives of the degrees of freedom,  $\dot{\underline{\eta}}$  and  $\dot{\underline{\chi}}$ .

$$E_\eta = \frac{1}{2} \dot{\underline{\eta}}^T \mathbf{M}_\eta \dot{\underline{\eta}} \quad E_b = \frac{1}{2} \dot{\underline{\chi}}^T \mathbf{M}_b \dot{\underline{\chi}} \quad (2)$$

Finally, the degrees of freedom can be rearranged into global stiffness and mass matrices,  $\mathbf{K}$  and  $\mathbf{M}$  respectively, and the vector of DOFs,  $\underline{\zeta}$ , defined in Equation 3. Therefore, the potential and kinetic energy of the beam,  $V_B$  and  $E_B$ , are defined by Equation 4.

$$\underline{\zeta} = \{\eta_1, h_1, \beta_1, \eta_2, h_2, \beta_2, \dots, \eta_{N_{nd}}, h_{N_{nd}}, \beta_{N_{nd}}\}^T \quad (3)$$

$$V_B = \frac{1}{2} \underline{\zeta}^T \mathbf{K} \underline{\zeta} \quad E_B = \frac{1}{2} \dot{\underline{\zeta}}^T \mathbf{M} \dot{\underline{\zeta}} \quad (4)$$

Structural damping of the main wing is accounted for by the introduction of damping proportional to the critical damping [15]. Given the matrices  $\mathbf{K}$  and  $\mathbf{M}$ , one can compute the corresponding undamped eigenvectors,  $\Phi$ , and eigenvalues,  $\underline{\lambda}$ , which are related to the natural frequencies of the system,  $\omega_n$ , presented in Equation 5 and Equation 6 respectively. Due to the orthogonality of the modes, the mass and stiffness matrix can be diagonalized to obtain the generalized matrices shown in Equation 7,  $\bar{\mathbf{K}}$  and  $\bar{\mathbf{M}}$ .

$$\Phi = \begin{pmatrix} \phi_{1,1} & \phi_{1,2} & \cdots & \phi_{1,3N_{nd}} \\ \phi_{2,1} & \phi_{2,2} & \cdots & \phi_{2,3N_{nd}} \\ \vdots & \vdots & \ddots & \vdots \\ \phi_{3N_{nd},1} & \phi_{3N_{nd},2} & \cdots & \phi_{3N_{nd},3N_{nd}} \end{pmatrix} \quad (5)$$

$$\underline{\lambda} = \{\omega_1^2, \omega_2^2, \dots, \omega_{3N_{nd}}^2\}^T \quad (6)$$

$$\bar{\mathbf{K}} = \Phi^T \mathbf{K} \Phi \quad \bar{\mathbf{M}} = \Phi^T \mathbf{M} \Phi \quad (7)$$

Defining the damping ratio,  $\xi_m$ , of the  $m^{\text{th}}$  mode, the generalized damping for a given damping ratio is defined in Equation 8. Finally, the damping matrix,  $\mathbf{C}$  is given by Equation 9. The damping of the system is fixed to  $\xi = 0.02$ , equivalent to a 2% of the critical damping.

$$\xi_m = \frac{\bar{C}_m}{2\bar{M}_m\omega_m} \Rightarrow \bar{C}_m = 2\bar{M}_m\omega_m\xi_m \quad (8)$$

$$\mathbf{C} = \Phi \mathbf{T}^{-1} \bar{\mathbf{C}} \Phi^{-1} \quad (9)$$

Finally, the initial beam properties, represented by  $\mathbf{K}$  and  $\mathbf{M}$ , are extracted from the Nastran model used in previous work [13]. The elastic axis is determined by applying the same procedure presented by Jrad et al. [16], and the beam stiffness and torsional properties are extracted using the tip unit loads procedure proposed by Elsayed et al. [17]. To conclude, the beam properties are adjusted to match the first five natural frequencies of the wing in the locked-hinge condition and the first two in the free-hinge condition, which were obtained in a Ground Vibration Test (GVT).

## 2. Wingtip: Rigid Body and Torsional Spring

The FFWT is defined as a rigid body connected to the last node of the beam using kinematic constraints and a torsional spring, with stiffness  $k_\theta$ , to simulate the locking mechanism. For sake of simplicity, two hinge conditions are considered: zero stiffness representing the free-hinge condition and high stiffness, three orders of magnitude above the bending stiffness of the wing, representing the locked-hinge condition.

Furthermore, as done by Healy et al. [18], from the structural point of view, the hinge is considered to have a zero flare angle to simplify the kinematic equations while still accounting for the torsional and bending deformation at the tip of the wing,  $\eta_h$  and  $h_h$ , and the total rotation angle of the FFWT,  $\gamma$ , which is a sum of the fold angle,  $\theta$ , and the slope angle due to bending at the tip node,  $\beta_h$ . Equation 10 presents the position of the FFWT center of gravity (CG),  $\underline{r}_{fwt}$ , with respect to the global coordinates system accounting for the kinematic constraints, where  $R_n(\mu)$  is a counterclockwise rotation around the corresponding axis,  $n$ . In addition,  $y'_{CG}$  and  $x'_{CG}$  represent the spanwise and chordwise distance of the FFWT CG to the elastic axis at the tip of the main wing expressed in local coordinates attached to the FFWT,  $x'y'z'$  in Figure 2.

$$\underline{r}_{fwt}(t) = \begin{Bmatrix} x_{fwt} \\ y_{fwt} \\ z_{fwt} \end{Bmatrix} = \begin{Bmatrix} 0 \\ B_h \\ h_h(t) \end{Bmatrix} + R_y(-\eta_t(t))R_x(\gamma(t)) \begin{Bmatrix} x'_{CG} \\ y'_{CG} \\ 0 \end{Bmatrix} \quad (10)$$

Therefore, the velocity,  $\underline{v}_{fwt}$  is obtained as a time derivative of Equation 10, which is then used in the kinetic energy term. In addition, the rotational term of the kinetic energy can be expressed in a body-fixed coordinate system, denoted  $x''y''z''$  in Figure 2, to simplify the corresponding equations. In this case, the angular velocity is expressed as a function of  $\gamma$  and  $\eta_h$ , as shown in Equation 11. Taking into account this consideration, the kinetic energy of the wingtip,  $E_{fwt}$ , is defined by Equation 12, where  $m_{fwt}$  is the mass of the FFWT obtained from the physical model and  $\mathbf{I}$  is the inertia tensor obtained from the CAD model and later modified to match the GVT results.

$$\underline{\underline{\Omega}}_{fwt}(t) = \begin{Bmatrix} \dot{\gamma} \\ \dot{\eta}_h \cos(\gamma) \\ \dot{\eta}_h \sin(\gamma) \end{Bmatrix} \quad (11)$$

$$E_{fwt} = \frac{1}{2} m_{fwt} \underline{v}_{fwt}^T \underline{v}_{fwt} + \frac{1}{2} \underline{\underline{\Omega}}_{fwt}^T \mathbf{I} \underline{\underline{\Omega}}_{fwt} \quad (12)$$

To conclude, the potential energy accounts for the elastic energy of the spring,  $V_K$ , and the gravity potential,  $V_g$ , which depend on the position of the wingtip as presented in Equation 13. Notice that gravity is defined in the spanwise direction to match the experiment [13]. Therefore, gravity acts as a restoring force, similar to the torsional spring.

$$V_{k_\theta} = \frac{1}{2}k_\theta\theta^2 \quad V_g = -m_{fwt}gy_{fwt}(\gamma, \eta_h) \quad (13)$$

### 3. Beam-FFWT System

The full system of equations can now be derived using the Euler-Lagrange method, where the generalized coordinates are the different DOFs of the beam,  $\eta_i$ ,  $h_i$ , and  $\beta_i$ , and the fold angle,  $\theta$ . The Lagrangian of the system is defined by Equation 14 and the EOM are defined by Equation 15, where  $\underline{\psi}$  and  $\underline{q}$  are the generalized coordinate vector and the vector of the external loads respectively. Therefore,  $\underline{q}$  comprises the aerodynamic forces and will be further developed in Section II.B.

$$\mathcal{L} = E_B + E_{fwt} - V_B - V_g - V_{k_\theta} \quad (14)$$

$$\frac{d}{dt} \left( \frac{\partial \mathcal{L}}{\partial \dot{\psi}_i} \right) - \frac{\partial \mathcal{L}}{\partial \psi_i} = q_i \quad i = 1, 2, \dots, 3N_{nd} + 1 \quad (15)$$

$$\underline{\psi} = \{\eta_1, h_1, \beta_1, \dots, \eta_{N_{nd}}, h_{N_{nd}}, \beta_{N_{nd}}, \theta\}^T$$

The resulting system of equations provides a set of linear equations defining the motion of the beam and four nonlinear equations corresponding to  $\theta$  and the three DOFs of the node at the tip of the beam, where the kinematic constraints between the main wing and the FFWT must be enforced.

## B. Aerodynamic Model

To complete Equation 15, it is necessary to define the generalized external forces, which are computed using quasi-steady aerodynamics strip theory. For the main wing, the generalized loads on the  $h_i$  and  $\eta_i$  DOFs are directly related to the lift and torsional aerodynamic moment. However, for the FFWT, the aerodynamic loads not only affect the DOFs at the tip of the main wing but also the  $\theta$  generalized coordinate. Therefore, the FFWT requires special treatment when developing the load terms [1].

In addition, the final objective of this study is to compare the nonlinear model with the results obtained in the wind tunnel. Therefore, a scaling factor is applied to the aerodynamic matrices to account for both the wing being partially immersed in the flow and the finite wing effects on the lift distribution.

### 1. Main Wing: Strip Theory

The aerodynamic loads acting on the main wing are implemented following the 2-DOFs wing section presented by Dimitriadis [19] and shown in Figure 3. The lift,  $l_i$ , and torsional moment,  $m_{a,i}$ , for each strip, corresponding to each of the structural elements, can be separated into circulatory (C) and non-circulatory parts (NC), as presented in Equation 16 and Equation 17, where  $b$  is the mid-chord point and  $a$  is the non-dimensional distance from the semi-chord to the elastic axis (EA).

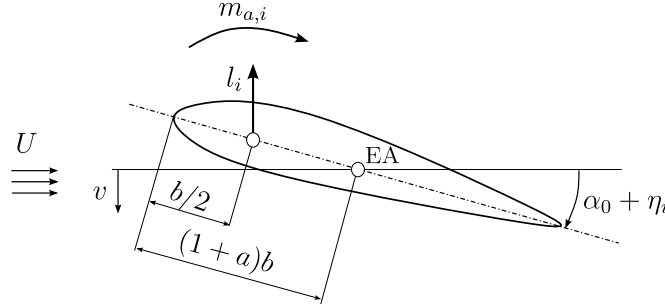


Fig. 3 Sketch of the 2-DOF airfoil section used in the strip theory aerodynamic model.

$$l_i = l_{nc} + l_c \quad m_{a,i} = m_{a,nc} + m_{a,c} \quad (16)$$



$$\begin{aligned}
l_{nc} &= \rho b^2 \pi (U \dot{\alpha} + \ddot{v} - b a \ddot{\alpha}) & l_c &= 2 \pi \rho b \alpha_i \\
m_{a,nc} &= \rho b^3 \pi \left( a \ddot{v} - U \left( \frac{1}{2} - a \right) \dot{\alpha} - b \left( a^2 - \frac{1}{8} \right) \ddot{\alpha} \right) & m_{a,c} &= 2 \pi \rho b^2 \left( a + \frac{1}{2} \right) \alpha_i
\end{aligned} \tag{17}$$

Notice that Figure 3 presents a different reference system than the one used in the structural model from Section II.A. Therefore, it is necessary to rearrange the matrices such that  $h = -v$ . In addition, the loads are considered constant in each strip, hence they are distributed among the nodes of each element and their respective DOFs. Finally, the local angle of attack at each strip,  $\alpha_i$ , is defined by Equation 18, where  $\alpha_0$  is the angle of attack at the root of the wing and  $U_g$  is the 1-cosine vertical gust airspeed.

$$\alpha_i = \alpha_0 + \eta_i + b \left( \frac{1}{2} - a \right) \dot{\eta}_i + \frac{\dot{v}}{U} + \frac{U_g}{U} \tag{18}$$

## 2. Wingtip: Adapted Strip Theory

The aerodynamic loads acting on the wingtip,  $l_{fwt}$  and  $m_{a,fwt}$ , are derived similarly to Section II.B.1. The wingtip is divided into  $N_{fwt}$  aerodynamic nodes that are loaded with the lift and moment presented in Equation 16 and 17. However, a local angle of attack,  $\alpha_{fwt}$ , defined by Equation 19, is used instead of the previous  $\alpha_i$  to account for the rotation of the wingtip.

$$\alpha_{fwt} = \alpha_g - \arctan \left( \frac{W}{U} \right) \tag{19}$$

On the one hand,  $\alpha_g$  represents the geometrical angle of attack defined using the geometrically exact representation of the local angle of attack presented by Healy et al. in Equation 20 and Equation 21 [18]. This representation conducts a series of rotations on the global velocity vector, defined by  $U$  and  $U_g$ , to account for the root angle of attack,  $\alpha_0$ , the deflections at the tip of the main wing,  $\beta_h$  and  $\eta_h$ , the flare angle of the hinge,  $\Lambda$ , and the fold angle,  $\theta$ . The result is the velocity vector in FFWT local coordinates,  $\underline{v}_f$ , from which  $\alpha_g$  is the angle of attack in the plane normal to the FFWT axis, defined by the  $z$  and  $x$  components of the velocity vector.

$$\underline{v}_f = \begin{Bmatrix} v_{f,x} \\ v_{f,y} \\ v_{f,z} \end{Bmatrix} = R_z(-\Lambda) R_x(\theta) R_z(\Lambda) R_x(\beta_h) R_y(\alpha_0 + \eta_h) [U, 0, U_g]^T \tag{20}$$

$$\alpha_g = \arctan \left( \frac{v_{f,z}}{v_{f,x}} \right) \tag{21}$$

On the other hand,  $W$  in Equation 19, represents the local normal velocity at a given distance from the hinge,  $d_i$ , and is defined by Equation 22, where  $d_a$  is the distance between the elastic axis and the 3/4 chord point, and  $\dot{h}^*$  and  $\dot{\alpha}^*$  are defined by Equation 23. In addition, the non-circulatory part of the load is approximated using Equation 17 but replacing  $\dot{h}$  and  $\dot{\alpha}$  with  $\dot{h}^*$  and  $\dot{\alpha}^*$  respectively.

$$W(\dot{h}^*, \dot{\alpha}^*, d_i) = -\dot{h}^* - \dot{\alpha}^* d_a \tag{22}$$

$$\dot{h}^* = -\dot{h}_t \cos(\gamma) - \dot{\gamma} d_i \quad \dot{\alpha}^* = \dot{\alpha}_g \tag{23}$$

Finally, the loads can be integrated along the wingtip to obtain the total aerodynamic loads acting on the tip node of the main wing. The loads  $M_\eta$ ,  $F_h$  and  $M_\theta$ , corresponding to  $\eta_h$ ,  $h_h$  and  $\theta$  generalised coordinates, are then defined by Equation 24. Notice that  $M_\eta$  and  $F_h$  are the result of projecting the total loads on the global reference frame used in the structural model.

$$\begin{aligned}
M_\eta &= \cos(\gamma) \int_0^{B_{fwt}} m_{a,fwt}(d_i) dd_i \\
F_h &= \cos(\gamma) \int_0^{B_{fwt}} l_{fwt}(d_i) dd_i \\
M_\theta &= \int_0^{B_{fwt}} d_i l_{fwt}(d_i) dd_i
\end{aligned} \tag{24}$$

### 3. Aerodynamic Scaling Factors

The scaling factors applied to the aerodynamic loads account for both the effects of the wing being partially immersed in the flow and the finite wing aerodynamic distribution. On the one hand, part of the wing is outside of the flow hence no aerodynamic loads are acting on it. This is accounted by the scaling factor,  $f_s$ , defined by Equation 25, where  $B_{lim}$  is the  $y$  coordinate at which the wing starts being immersed in the flow.

$$f_s(y) = \begin{cases} 0 & \text{if } y < B_{lim} \\ 1 & \text{if } y \geq B_{lim} \end{cases} \tag{25}$$

On the other hand, an elliptic lift distribution, which is representative of the lift distribution over a finite wing [1], is enforced with the factor,  $f_e$ . However, given that whether the hinge is free or locked affects the lift distribution, as presented by Healy et al. [18], two different distributions are considered. When the hinge is locked, one elliptic lift scaling distribution is applied to the whole wing, including the FFWT, as defined by Equation 26. However, when the hinge is free, the load scaling distribution is defined by Equation 27: one elliptic distribution is considered up to the hinge while a second scaling distribution is applied over the FFWT.

$$f_{e,locked}(y) = D_1 \sqrt{1 - \left(\frac{y}{B_{tot}}\right)^2} \text{ for } 0 < y < B_{tot} \tag{26}$$

$$f_{e,free}(y) = \begin{cases} D_2 \sqrt{1 - \left(\frac{y}{B_{tot}}\right)^2} & \text{if } y < B_h \\ D_3 \sqrt{1 - \left(\frac{y-B_h}{B_{tot}-B_h}\right)^2} & \text{if } B_h < y < B_{tot} \end{cases} \tag{27}$$

Notice that each of these distributions is scaled by a factor,  $D_i$ , that determines the maximum achievable lift. Due to the combination of the open wind tunnel section and the impact of the wingtip on the lift distribution, these constants cannot be easily determined a priori. Instead, it was decided to optimize them to match the bending loads and fold angle from the experimental steady-state measurements as presented in Section III.B. The resulting values used in this study are presented in Table 1.

**Table 1 Optimised values of elliptic distribution constants**

Constant	$D_1$	$D_2$	$D_3$
Value	0.71	0.35	0.60

Finally, the total factor,  $f_i$ , is the product of both components,  $f_s$  and  $f_e$ , as presented in Equation 28 with the resulting scaling distributions presented in Figure 4.

$$f_i(y) = f_s(y)f_e(y) \tag{28}$$

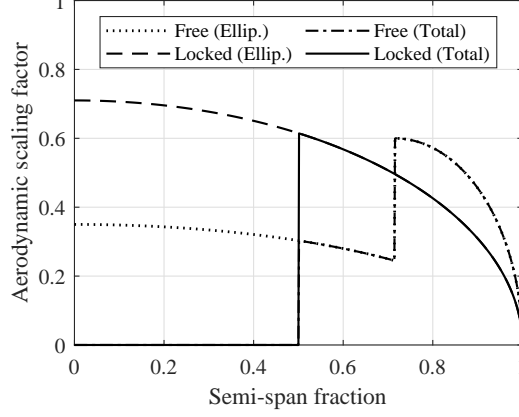


Fig. 4 Spanwise distribution of the total mask factor,  $f_i$ , and the elliptical mask factor,  $f_e$ .

### C. Aeroelastic Model

The full aeroelastic model can be assembled into a nonlinear state-space model due to the nonlinear behavior of the FFWT. Hence, the state matrix,  $\mathbf{A}$ , is a function of the states of the system. The final system can be represented by the nonlinear system defined in Equation 29. Nevertheless, the problem is solved using Taylor series expansion to linearize the system. The state about which the system is linearized depends on the analysis, as presented in the following subsections. Finally, the equivalent linearized state-space system is presented in Equation 30.

$$\mathbf{M}(\underline{\psi}, \underline{\dot{\psi}}, \underline{\ddot{\psi}}) \underline{\ddot{\psi}} + \mathbf{C}(\underline{\psi}, \underline{\dot{\psi}}, \underline{\ddot{\psi}}) \underline{\dot{\psi}} + \mathbf{K}(\underline{\psi}, \underline{\dot{\psi}}, \underline{\ddot{\psi}}) \underline{\psi} = \underline{q}(t, \underline{\psi}, \underline{\dot{\psi}}, \underline{\ddot{\psi}}) \quad (29)$$

$$\begin{pmatrix} \underline{\ddot{\psi}} \\ \underline{\dot{\psi}} \end{pmatrix} = \mathbf{A}(\underline{\psi}, \underline{\dot{\psi}}, \underline{\ddot{\psi}}) \begin{pmatrix} \underline{\dot{\psi}} \\ \underline{\psi} \end{pmatrix} \Big|_0 + \underline{B}(t) \quad (30)$$

#### 1. Steady-State Solution

Due to the nonlinearity of the system and the linear methodology used to solve it, the problem has to be solved iteratively. This is done following the Newton-Raphson method, presented in the block diagram of Figure 5. First, the state variables are initialized in the undeformed position. Afterward, the state-space system is assembled by linearizing around the initialized variables. Next, the static problem can be solved to obtain a new value of the state variables. Finally, the new values are compared to the initial value using the root of the square error in order to check the convergence of the solution with a convergence threshold,  $\delta$ . If it is not converged, the state-space system is reassembled with the linearization around the new state variables.

#### 2. Time-Marching Solution

The time response of the system is obtained using Time-Varying Linear Approximation (TVLA). This method approximates the nonlinear system with a set of linear equations with time-varying coefficients. As reported by Dimitriadis [19], TVLA is not the most efficient method but is more robust than first-order integration methods, such as the Euler method. An interesting feature of the method is that the eigenvalues and eigenvectors pertinent to the linearized system,  $\underline{\lambda}$  and  $\underline{\Phi}$  respectively, are available at every time step, which provide means of assessing the time evolution of the system's stability. A detailed explanation of the method and its derivation is given by Dimitriadis [19].

In the current work, this method is applied in combination with an initial steady-state simulation to obtain the time response of the folding wingtip. The block diagram of the time-marching solution is presented in Figure 6. First, the steady-state for given initial conditions is calculated to determine the value of the state variables at  $t_0$ . Afterward, as done for the steady state, these variables are used to assemble the state-space

system. Next,  $\underline{\lambda}$  and  $\underline{\Phi}$  are used to obtain the state variables at the instant  $t_{i+1}$ . To conclude, the instant  $t_{i+1}$  is used as  $t_i$  for the next time-step,  $\Delta t$ , and the procedure is repeated until  $t_{final}$  is achieved.

### 3. Modal Analysis

Modal analysis is conducted on the system matrix,  $\mathbf{A}$ , with two objectives: the model update using GVT results and the linear flutter analysis. For the comparison with the results of the GVT, the airspeed is set to zero, and an eigenvalue analysis is conducted. The resulting modal parameters are calculated using Equation 31, where  $\xi_n$  is the damping ratio and  $\omega_n$  is the natural frequency. For the flutter analysis, the same procedure is applied at different speeds in which the eigenvalue analysis is conducted around the steady state pertinent to the given flow conditions, similar to the procedure presented by Healy et al. [20].

$$\lambda_n = a_n \pm ib_n \Rightarrow \begin{cases} \xi_n = \frac{a_n}{\sqrt{a_n^2 + b_n^2}} \\ \omega_n = |b_n| \text{ [rad/s]} \end{cases} \quad (31)$$

### 4. Nonlinear Stability Analysis

Although the linear stability analysis on the nonlinear static solution presented in Section II.C.3 can provide a good prediction of the aeroelastic stability of the system, the observations in the experimental work [13] and other references [18] suggest that the nonlinear nature of the system will lead to LCOs.

For this reason, the time-marching solution is also used to assess the occurrence and development of LCOs, taking advantage of the local stability analysis necessary for the TVLA method. In this context, the time-marching solution is used to study how the amplitude of the LCOs develops with increasing velocity in a bifurcation diagram, which will also allow a comparison of the nonlinear bifurcation point with the linear flutter speed obtained with the modal analysis.

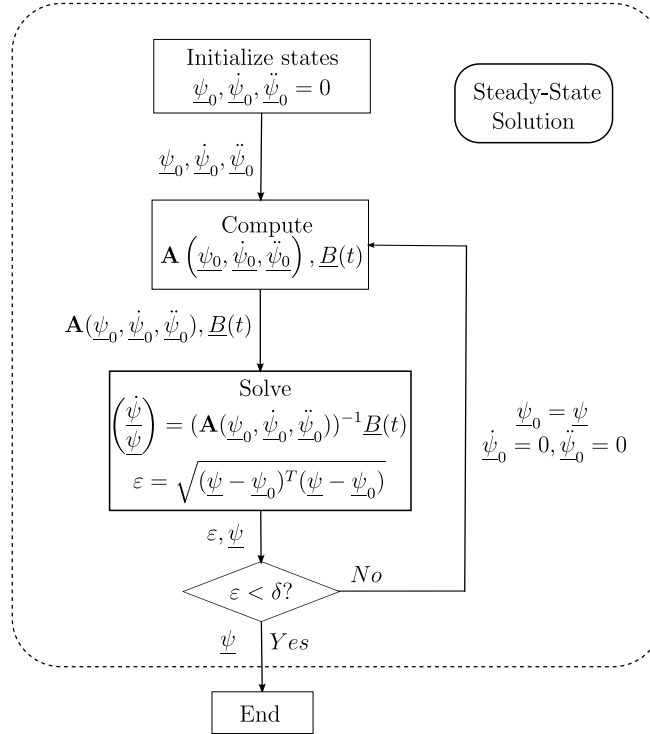


Fig. 5 Block diagram of the steady-state solver.



### III. Results

The results of the different numerical analyses are presented in this section. First, the modal analysis is used to update the structural properties. Next, the results of the steady-state analysis used to adjust the aerodynamic properties are presented and compared to the experimental values presented in previous work [13]. Next, the dynamic behavior of the wing is studied by analyzing the gust response and the GLA performance of the FFWT. Finally, the stability of the system is studied with a linear flutter analysis and a nonlinear stability analysis investigating the LCO behavior and pertinent bifurcation diagram.

To conclude, a summary of the numerical input values used in this study is presented in Table 2. These values are selected considering a trade-off of, on the one hand, the convergence of the results and, on the other hand, the computational time required to solve the problem.

**Table 2 Input constants used in the numerical analysis**

Constant	$N_{el}$	$N_{nd}$	$N_{DoF}$	$N_{fwt}$	$\delta$	$\Delta t[s]$
Value	20	21	64	21	0.001	0.001

#### A. Modal analysis

As explained in Section II.C.3, the model is updated to match the modal analysis with the GVT. The final results of the structural modal analysis are presented in Table 3, where the natural frequencies of the numerical model are compared to the experimental values from the GVT. In this table and further discussions, the out-of-plane modes will be referred to as bending modes (B) in the locked-hinge condition and flapping modes (F) in the free-hinge condition, while no distinction will be made for the torsional mode (T).

In general, the numerical model shows good agreement with the experiment with relative differences below 5%. The exceptions are the 3rd bending natural frequency (3B) and the 1st flapping (1F), which present higher differences. On the one hand, the difference in the 3B frequency is of the order of 30%. However, the 3B mode is not involved in the flutter mechanism, as will be seen later in Section III.D.1. In addition, the gust frequencies are far below the 3B frequency. Therefore, this difference should have a limited impact on the stability of the system and the dynamic gust response. On the other hand, the relative difference in 1F frequency is of the order of 15% but the absolute difference is of the order of 0.2 Hz, which is a reduced difference of the same order as the other modes.

**Table 3 Comparison of the experimental natural frequencies of bending (B), torsion (T) and flapping (F) modes with the numerical results.**

Condition	Locked				Free	
Mode	1B	2B	1T	3B	1F	2F
Experimental [Hz]	3.52	21.50	43.06	47.46	1.33	4.40
Numerical [Hz]	3.67	22.35	45.12	61.44	1.14	4.48
Difference [%]	4.25	3.95	4.78	29.47	-14.68	1.88

#### B. Steady-State

As explained in Section II.B.3, the steady-state results are used as a reference to determine the aerodynamic constants of the scaling factors. Figure 7 presents the results with the parameters given in Table 1, which show a good agreement between the experimental and numerical results, with relative differences of the order of  $\pm 5\%$  with respect to the experiment.

Additionally, it is important to remark that the experimental results have been shifted in the horizontal axis such that a  $\alpha_0 = 0^\circ$  results in zero bending load. This correction is done to account for the uncertainty of the experimental  $\alpha_0$  measurement taking into account that the wing has a symmetric profile and was

mounted vertically, hence no bending loads are expected at this angle of attack. This way, when assessing the dynamic response in the following sections, it is possible to find the equivalent  $\alpha_0$  at which the experiment was conducted by looking at the steady-state loads before and after the gust.

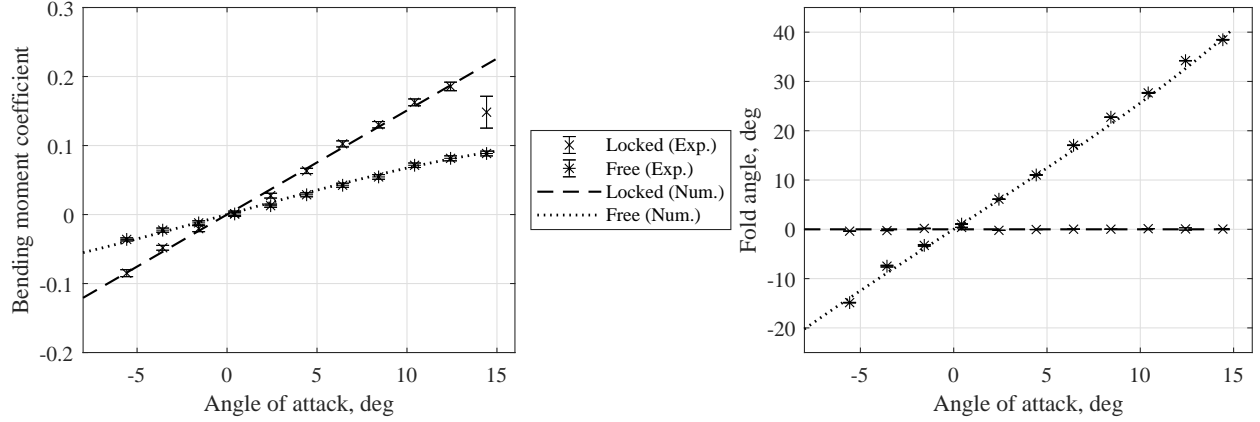


**Fig. 7 Comparison of  $C_B$  and  $\theta$  polars between numerical (num.) model and experimental (exp.) values.**

### C. Gust Response

The test cases presented in the previous sections have been used to calibrate the numerical model with experimental data. However, the main challenge is to accurately predict the dynamic response of the aeroelastic FFWT system. Therefore, the response of the wing to 1-cosine gusts and the GLA performance are addressed in this section.

#### 1. Response to 1-Cosine Gusts

The results of the time response of the wing facing 1-cosine gusts are compared in this subsection. For the sake of simplicity, only two different frequencies and three hinge conditions at an equivalent  $\alpha_0 = 6^\circ$  have been considered for this comparison. The selected frequencies are 0.5 Hz and 8 Hz, equivalent to reduced frequencies,  $k$ , of 0.014 and 0.220, which are representative of a quasi-steady case and a highly unsteady case respectively. When it comes to hinge release instants, three cases are considered: the free-hinge, in which the FFWT is free to rotate, the locked-hinge, in which the hinge is locked and the system acts as a regular wing, and the 0% release, which is the name given to the instant at which the gust hits the wing.

Figure 8 presents the results for the quasi-steady conditions of the 0.5 Hz gust. One can observe that the steady loads in both locked-hinge and free-hinge conditions are in good agreement with the experimental results, as expected due to the results of Section III.B. On the other hand, the dynamic loads present some differences. First of all, the gust profile is not an exact 1-cosine gust due to the wake shedding of the gust vanes, previously reported by Geertsen [23], which causes differences in the dynamic response. Secondly, the maximum loads are underpredicted by the numerical model between 10% and 15% with respect to the experimental maximum loads, which could be caused by the already mentioned differences in the gust profile. Finally, the 0% release condition presents more prominent oscillations than the experimental results, which shows an underprediction of the damping in the numerical model.

When it comes to the fold angle, the free-hinge and 0% release responses show good agreement with the experiment but there is an offset of  $2^\circ$  with respect to the experiment. Given the consistency of this offset, it might be explained by experimental reasons such as an offset in the fold angle measurements or small differences in the modelling of the hinge, such as the lack of friction in the hinge of the numerical model. Nevertheless, the results show good agreement with the experiment and the trends observed in the experiment are well reproduced in the numerical results.

Next, Figure 9 presents the results for the highly unsteady conditions of the 8 Hz gust. In this case, there is good agreement of the bending moment and the amplitude of the oscillations of the fold angle.

Nevertheless, there seems to be a small difference in the dynamics of the FFWT, which, causes a noticeable difference in the fold angle response. The response in the numerical model seems to be a superposition of two oscillatory signals of different frequencies. These oscillations are aligned such that some of the negative peaks in the bending moment are amplified, as can be seen in Figure 9e. When looking at the fold angle, this alignment produces an out-of-phase response. Since this is a highly unsteady case, these differences in the dynamic response could be caused by the limitations of the quasi-steady aerodynamics model. In the case of the 0% release, there is a second potential source of discrepancies, which is the change in the aerodynamic loads. As explained in Section II.B.3, the aerodynamic distribution changes between locked-hinge and free-hinge conditions, hence there is a change of load distribution in the 0% release case. Therefore, at the release instant, there is a discontinuity in the aerodynamic forces caused by the instantaneous change of the aerodynamic distribution.

In summary, the numerical model is capable of capturing the main features of the dynamic response, such as the peak loads and the increase in the persistence of the oscillations with dynamic hinge release. However, there are still some differences in the fold angle response, which might be caused by the limitations of using quasi-steady aerodynamics, the discontinuity in the loads caused by the change of aerodynamic distribution, and the uncertainties from the experimental measurements. In the future, the implementation of unsteady aerodynamics and a continuous transition of the aerodynamic distribution could provide more refined predictions by the numerical model.

## 2. GLA Performance

Next, the proposed aeroelastic model is used to repeat the GLA performance study and compare it to the experimental results. Figure 10 presents the comparison of the relative peak load reduction between the experiments and the numerical model. The numerical results present the same trends as the experiment for all of the gust frequencies: an early hinge release can provide load alleviation but releasing the hinge too late can actually increase the peak loads. Nevertheless, there are some differences in the results when the hinge is released during the gust (0%, 50%, and 100% release): the relative peak load reduction is, in general, lower in the numerical model but, for the 0% release, the reduction is up to 40% higher than in the experiment for the gust frequencies of 3.5 Hz, 5 Hz, and 8 Hz. To explain these differences, two possibilities are considered. On the one hand, the experimental work showed a study of the uncertainty in the hinge release instant and its impact on the effective release [13]. Due to this uncertainty, it is hard to align the numerical and the experimental hinge release instants. Therefore, even though the average delays obtained in the experiment are taken into account, there is still some uncertainty as to when the hinge is effectively released. On the other hand, the discontinuity on the aerodynamic loads mentioned in Section III.C.1 affects all the cases with an active release, so it might also contribute to the differences in the peak loads.

When looking at the relative root mean square (RMS) results, presented in Figure 11, the results show similar trends as the experiment. The numerical results show good agreement with the experiment, although the highest relative RMS is in general higher in the numerical model. However, there are important differences in the free-hinge and pre-release conditions for 3.5 Hz, 5 Hz, and 8 Hz gusts, corresponding to reduced frequencies of 0.096, 0.137, and 0.220 respectively. In these cases, the relative RMS is up to 50% higher than the experiment, even higher than in the locked case, which can be caused by the quasi-steady aerodynamics model. As mentioned in Section III.C.1, the quasi-steady assumption does not hold at high gust frequencies. Since the differences start to appear at 3.5 Hz, above the limit between quasi-steady and unsteady aerodynamics of  $k = 0.05$ , the aerodynamic model might play a role in the discrepancies between the numerical results and the experimental ones.



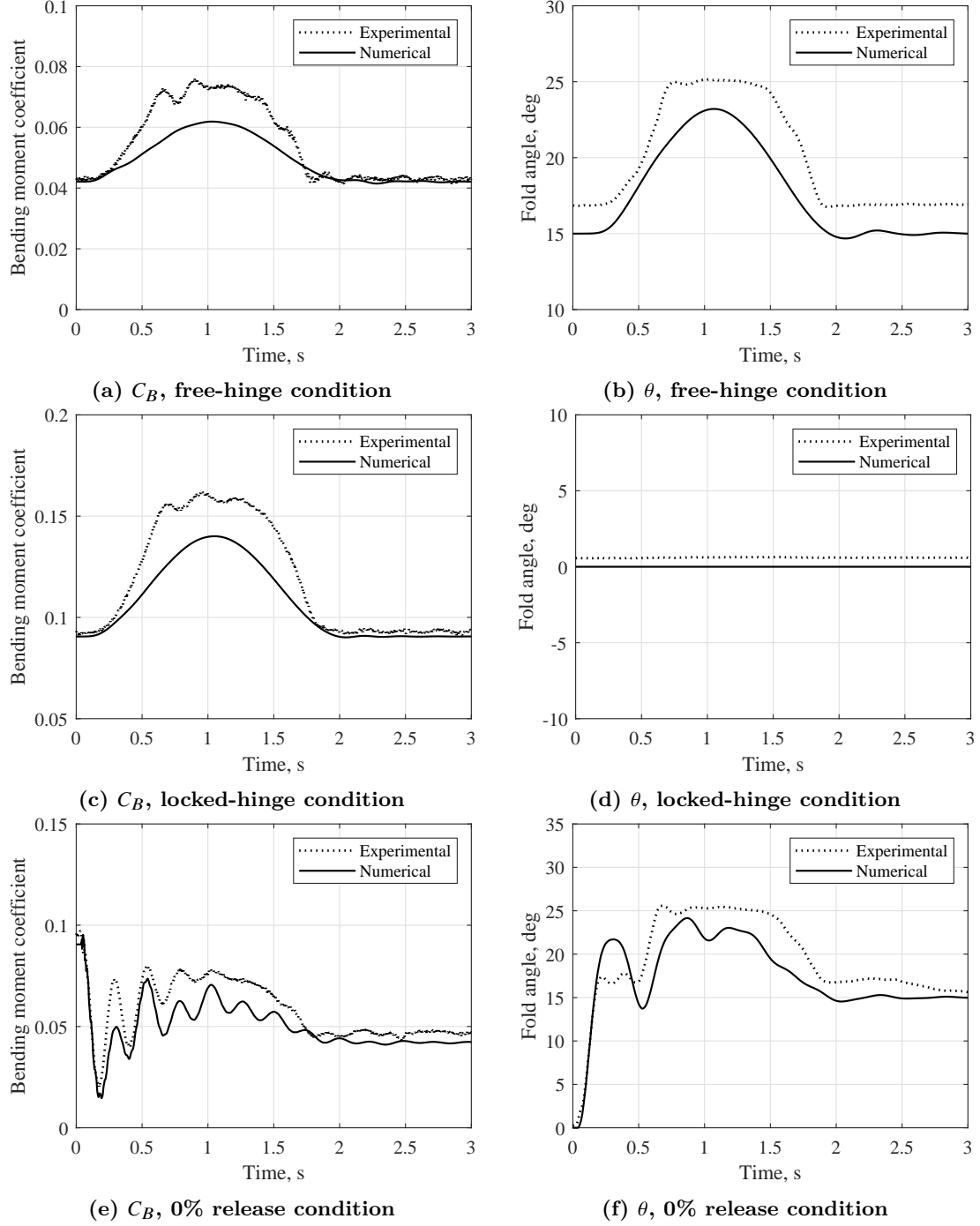


Fig. 8 Time response to a 0.5 Hz 1-cosine gust

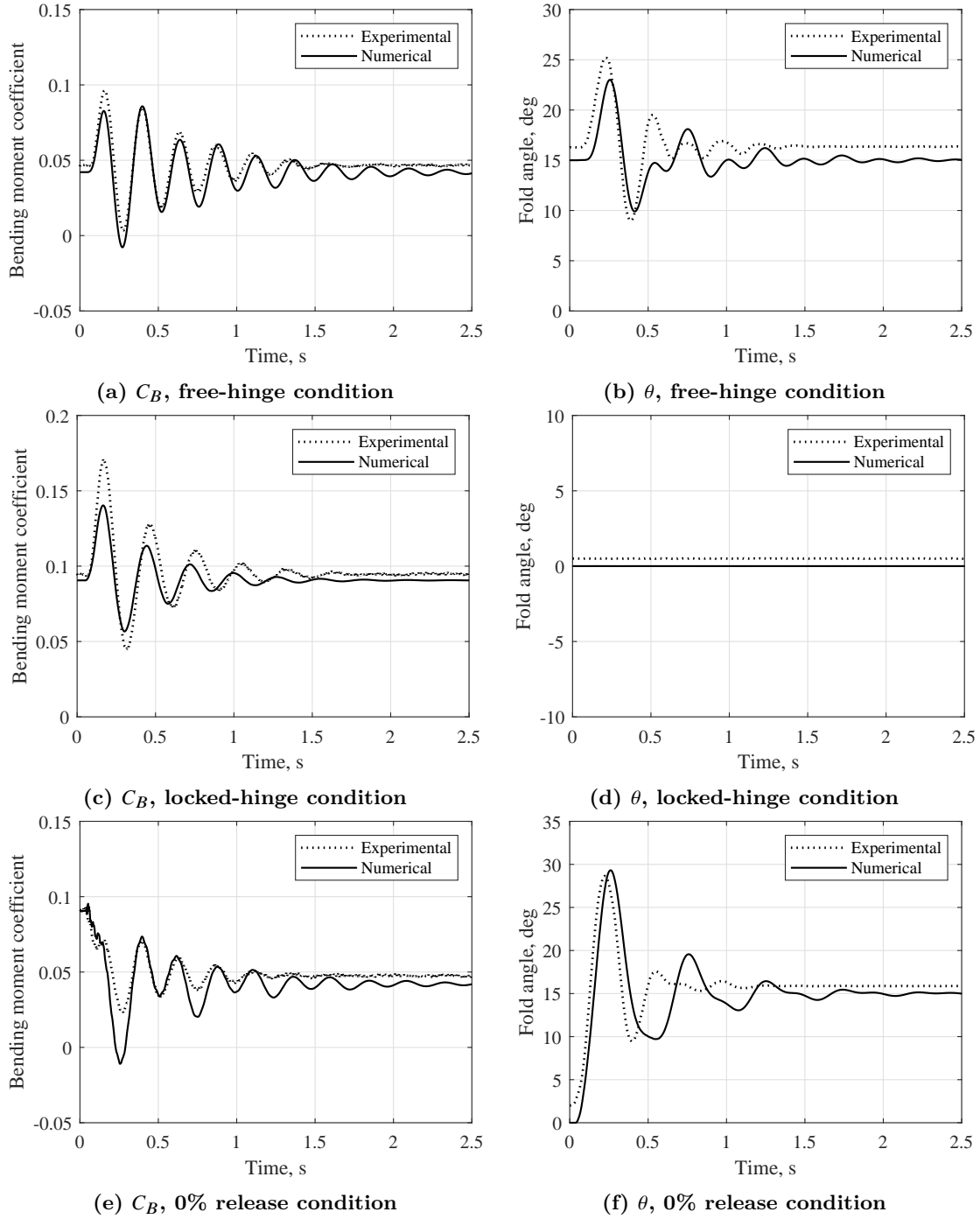
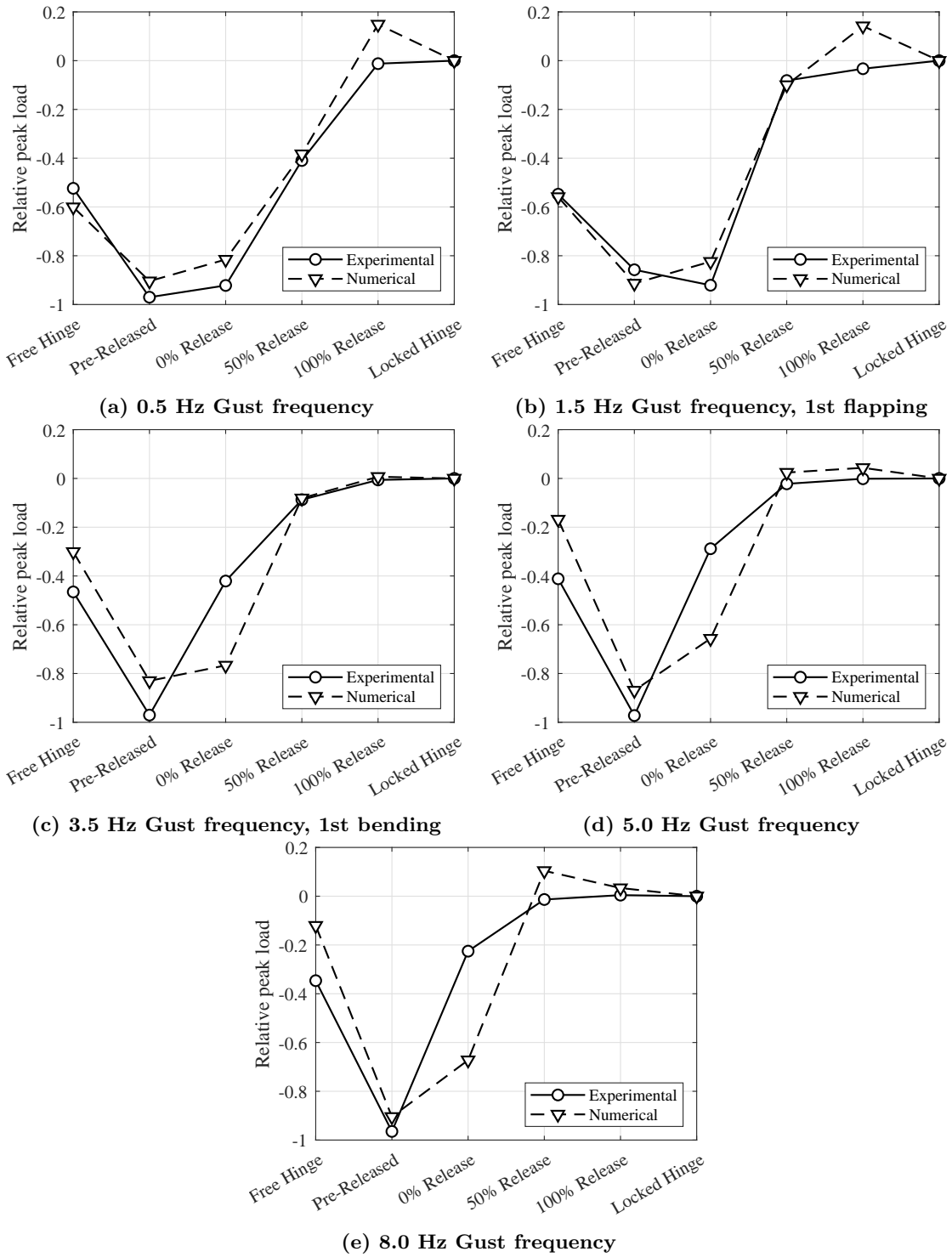


Fig. 9 Time response to a 8 Hz 1-cosine gust



**Fig. 10** Relative peak load reduction with respect to peak load in locked-hinge condition at  $\alpha_0 = 6^\circ$

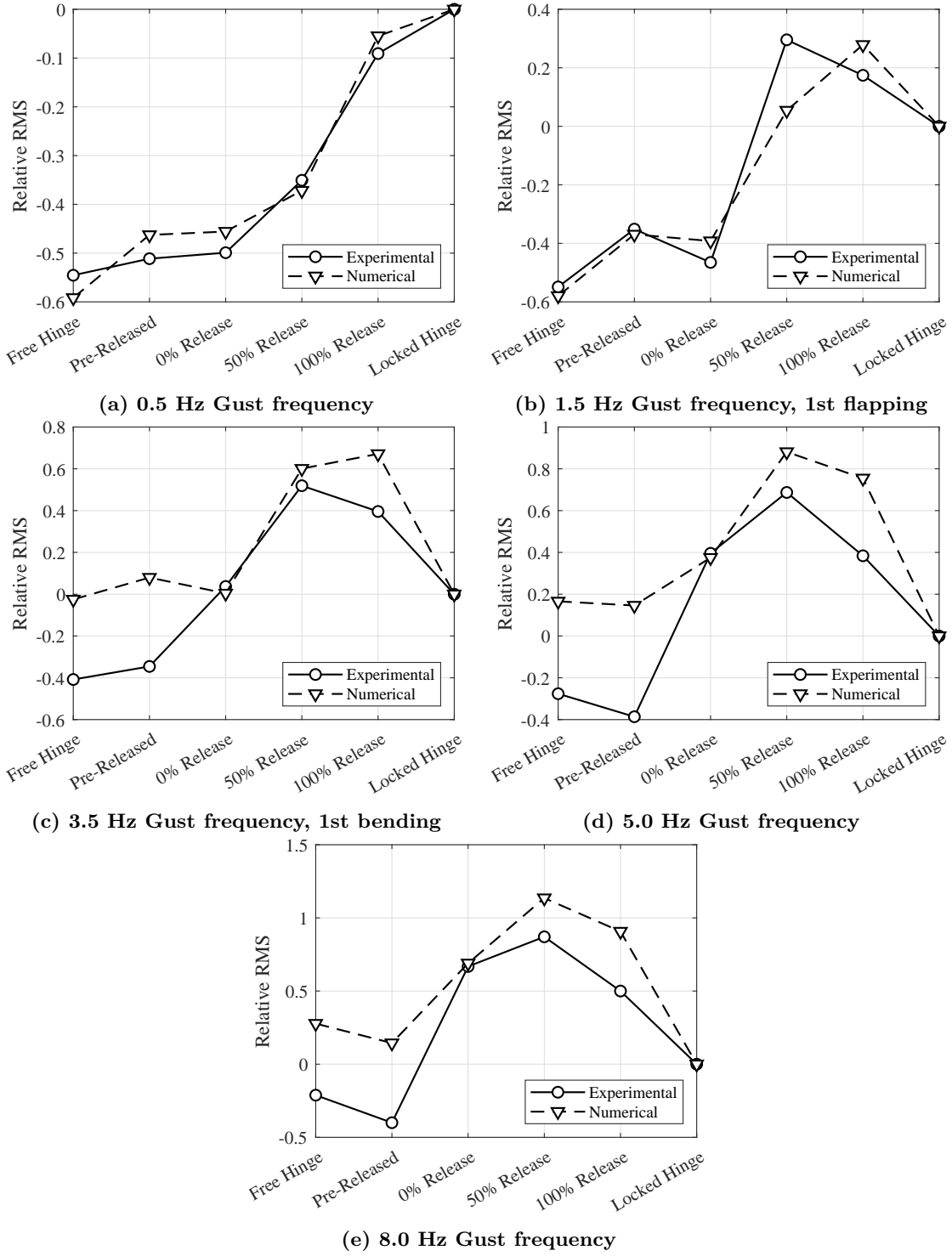


Fig. 11 Relative RMS reduction with respect to RMS in locked-hinge condition at  $\alpha_0 = 6^\circ$

## D. Stability analysis

Finally, the stability of the system can be addressed using different approaches. On the one hand, the linear flutter onset is studied using modal analysis around the corresponding steady-state at each airspeed. On the other hand, the time domain solver is used to assess the nonlinear stability and the occurrence of LCOs.

### 1. Linear Flutter Onset

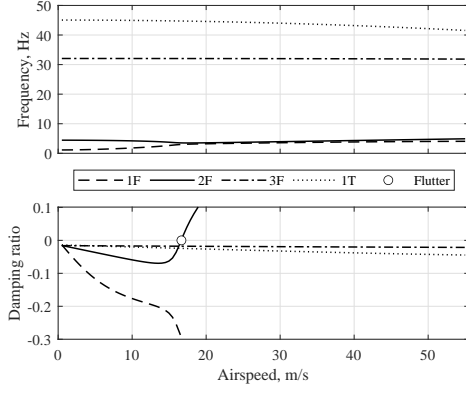
After ensuring the similarity of the modal properties between the numerical model and the experiment, it is now possible to assess the linear flutter boundary as a function of the angle of attack. Figure 12, 13 and 14 present the  $V - g$  and  $V - f$  plots at  $\alpha_0 = 0^\circ$ ,  $\alpha_0 = 5^\circ$  and  $\alpha_0 = 10^\circ$  respectively.

On the one hand, in the free-hinge condition, the flutter mechanism is an interaction between the 1F and 2F modes, which makes the 2F mode unstable. Looking at the effects of  $\alpha_0$ , the flutter speed increases from 16.6 m/s at  $\alpha_0 = 0^\circ$  to 17.2 m/s at  $\alpha_0 = 5^\circ$  and 19.8 m/s at  $\alpha_0 = 10^\circ$ . This increase in the flutter onset velocity is the result of the combination of gravity and the change in the inertia properties of the aeroelastic system. On the one hand, gravity acts similarly to a torsional spring on the  $\theta$  DOF, since the force is proportional to the out-of-plane distance between the FFWT CG and the hinge, hence increases with  $\theta$ . On the other hand, the FFWT deflection changes the mass distribution, so the inertia properties of the wing are also affected by a change in  $\theta$ . The combination of these effects can be visualized in Figure 15a, which presents a ratio of the frequencies of the flutter mechanism, 2F/1F, as a function of  $\theta$  for  $U = 0$  m/s. As can be seen, the frequency ratio increases with the FFWT deflection, so the modes separate from each other.

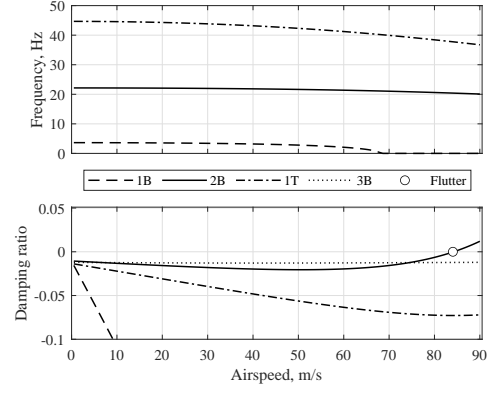
Furthermore, to visualize how each case is affected by the airspeed, Figure 15b presents the same frequency ratio for the different  $\alpha_0$  and the corresponding  $\theta$  deflection. At low speeds, where  $\theta$  is below  $30^\circ$ , the angle of attack barely affects the ratio. However, when the airspeed increases, the aerodynamic loads become more important, producing  $\theta$  deflections above  $30^\circ$  at  $\alpha_0 = 10^\circ$ . As seen in Figure 15a, the modes involved in the flutter mechanism start separating when  $\theta$  is above  $30^\circ$ , so the energy required to make the wing unstable increases, which delays the flutter onset. In summary, the rate of decay of the frequency ratio decreases with the increasing  $\alpha_0$  due to the separation of the modes, which causes a delay of the flutter onset.

When compared to the experimental results shown in Figure 16 [13], the trends are reversed: the flutter speed in the experiment decreased when increasing  $\alpha_0$ . Although it is not clear what causes this difference, the experimental setup might be one of the reasons. As previously mentioned, the wing was not completely submerged in the flow and the test cases were chosen to keep the wingtip within the open jet. However, when assessing the flutter onset, this condition might have not been respected due to the high deflections in the out-of-plane direction. Since the aerodynamic scaling factors in the numerical model only account for the spanwise dimensions of the open jet, it is not possible to completely replicate the experimental case.

On the other hand, the locked-hinge condition presents the expected results. The 1T and the 2B modes are affected by the increase in  $\alpha_0$ , promoting flutter when increasing  $\alpha_0$ . Although the beam of this model is linear, the FFWT contribution to the mass matrix is updated accounting for the static deflections. Therefore, as previously reported by Tang and Dowell [21] or Drachinsky et al. [22] with the Pazy wing, which was used as a reference for the manufacturing of the experimental FFWT model, increasing the deflections promotes the flutter onset. Since the FFWT in locked-hinge condition acts similarly to a very flexible wing without a hinge, it was expected to find agreement between the results in the locked-hinge condition and those from reference very flexible wings.

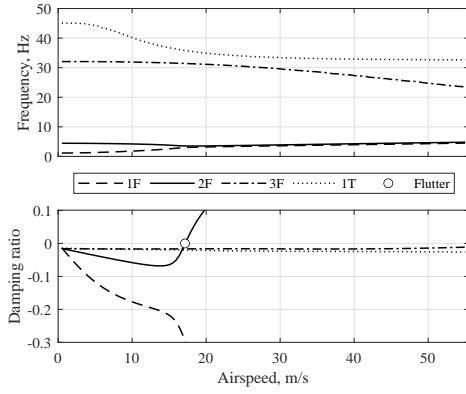


(a) Free hinge

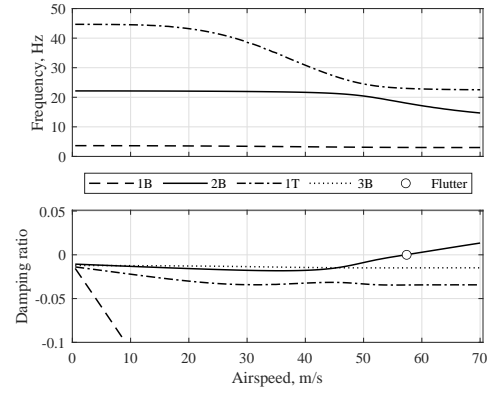


(b) Locked hinge

Fig. 12 Comparison of  $V - g$  and  $V - f$  flutter plots in free-hinge and locked-hinge conditions at  $\alpha_0 = 0^\circ$

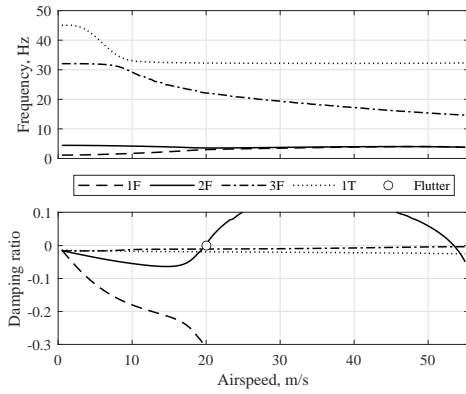


(a) Free hinge

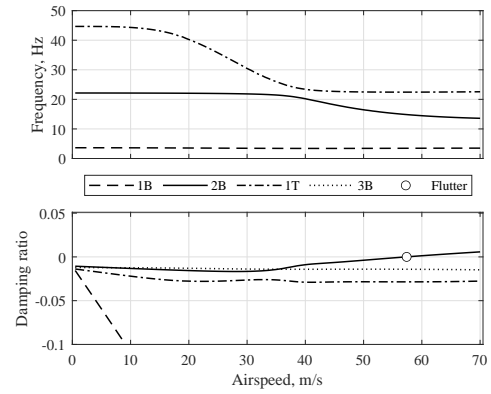


(b) Locked hinge

Fig. 13 Comparison of  $V - g$  and  $V - f$  flutter plots in free-hinge and locked-hinge conditions at  $\alpha_0 = 5^\circ$



(a) Free hinge



(b) Locked hinge

Fig. 14 Comparison of  $V - g$  and  $V - f$  flutter plots in free-hinge and locked-hinge conditions at  $\alpha_0 = 10^\circ$

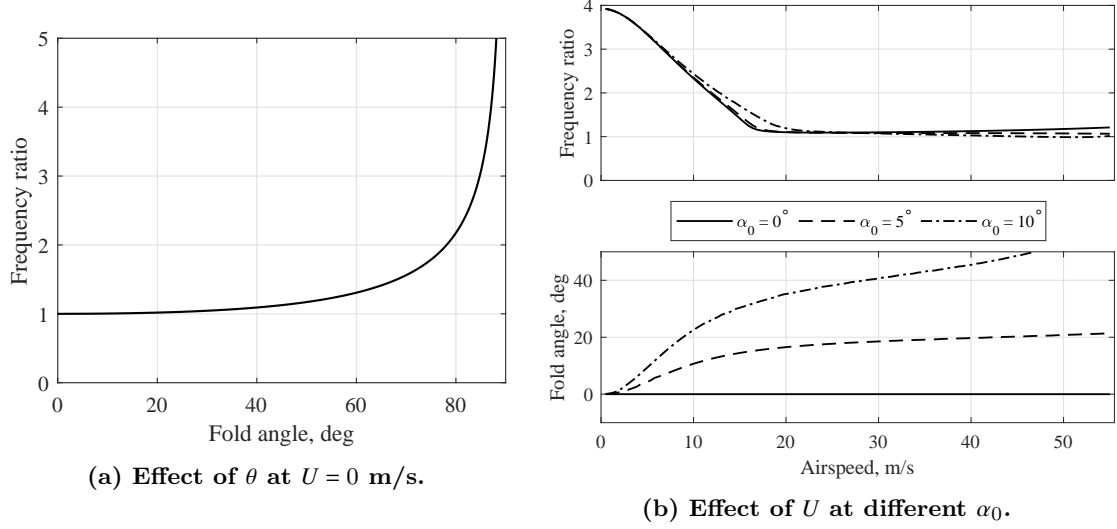


**Fig. 15** Study of the ratio between the second flapping frequency (2F) and the first flapping frequency (1F).

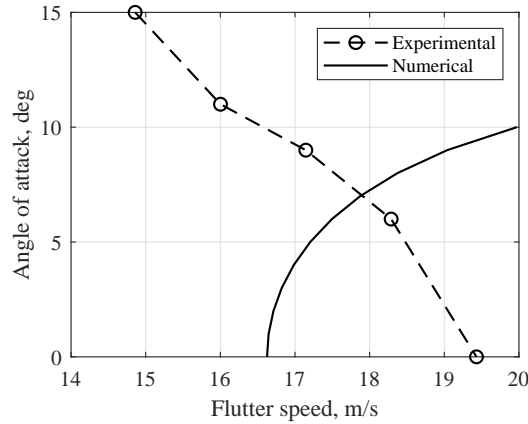


**Fig. 16** Comparison of the ratio between the second flapping frequency (2F) and the first flapping frequency (1F) for different  $\alpha_0$ .

## 2. Nonlinear Stability

To conclude the Results section, the stability of the system beyond the linear flutter onset velocity is presented. The TVLA time-marching analysis allows for studying the nonlinear effects on stability. Figure 17 presents the time response of the wing at  $U = 17 \text{ m/s}$  and  $\alpha_0 = 10^\circ$ , which is higher than the linear flutter onset velocity. In Figure 17a, the phase diagram shows how the wingtip starts oscillating and eventually stabilizes on a closed trajectory signifying the appearance of LCOs. On the other hand, Figure 17b presents the time response of the fold angle considering the instantaneous stability of the system. Initially, the wing is unstable, hence the damping over the entire cycle is negative. However, when the oscillations grow large enough, parts of the cycle exhibit positive damping. Once the energy inflow and outflow of the aeroelastic system are balanced, the system settles on a stable LCO of constant amplitude. This can be observed in the last cycles of the response, presented in Figure 17c, where the stable and unstable parts of the cycle remain constant.

Next, Figure 18 presents the bifurcation diagram of the fold angle at different  $\alpha_0$ . First, all the results exhibit a Hopf bifurcation, in which the branch corresponding to the steady state fold angle becomes unstable

when crossing the bifurcation velocity and separates into the two stable branches representing the maximum and minimum value of the fully developed LCO. Notice also that, due to the change in steady-state caused by the change in  $\alpha_0$ , the LCO occurs at different average deflections: at  $\alpha_0 = 0^\circ$  the FFWT oscillates around  $\theta = 0^\circ$  while at higher  $\alpha_0$  the FFWT oscillates around  $\theta > 0^\circ$ , the static solution.

Finally, Table 4 presents a comparison of the linear flutter speeds obtained in Section III.D.1 and the bifurcation speeds obtained from the bifurcation diagram. One can see that there is good agreement with the linear solution although the differences tend to increase with  $\alpha_0$ . It was expected that both analyses would coincide but, while the difference at  $\alpha_0 = 0^\circ$  is negligible, there is a 9% difference at  $\alpha_0 = 10^\circ$ . However, looking again at Figure 17b, one may notice that the stability of the system is not only determined by the deflection but also by the rate of change of the deflection: if the stability was dominated by the deflection, the system would be stable above a certain threshold and unstable otherwise, which is not the case. Therefore, the rate of change also plays a role in the stability of the system. Since the linear flutter analysis assumes a steady state ignoring the rates of change, this might be the cause of these differences. Nevertheless, it will be further investigated in the future.

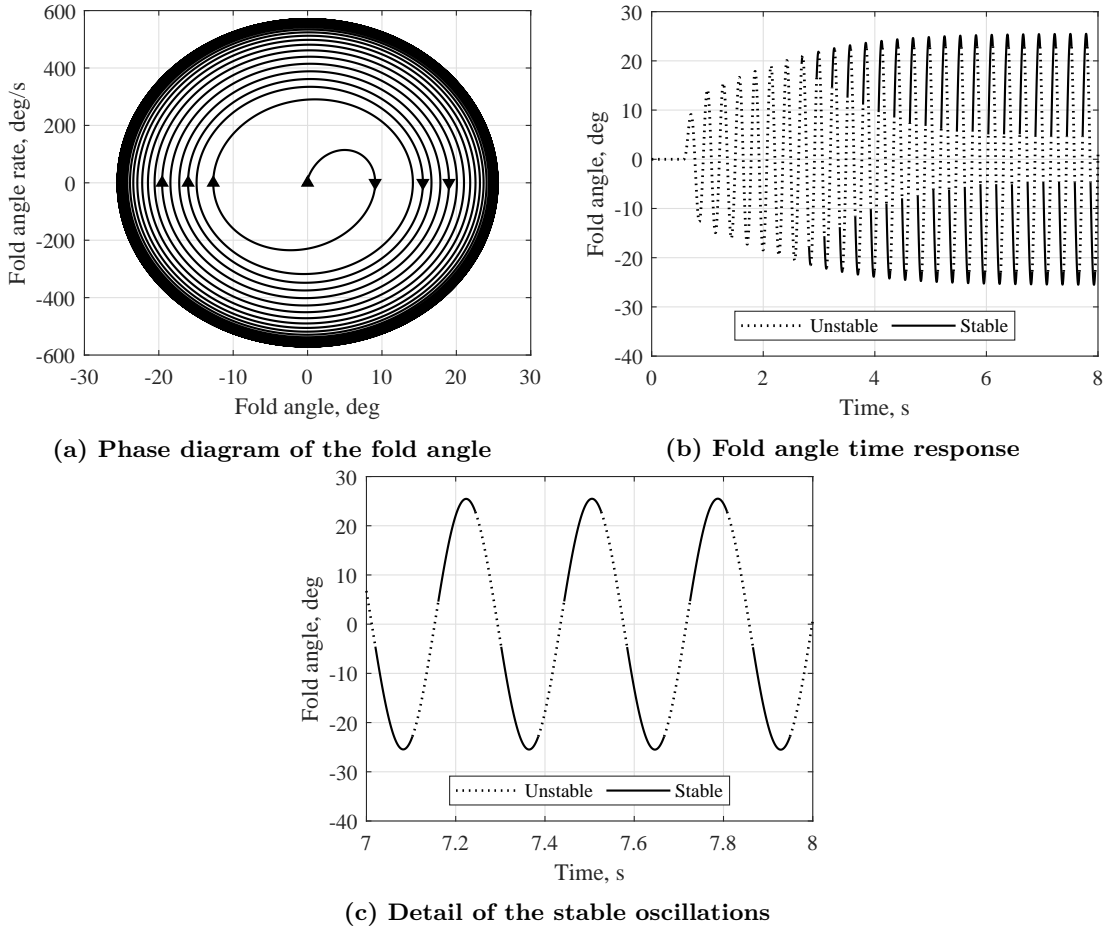
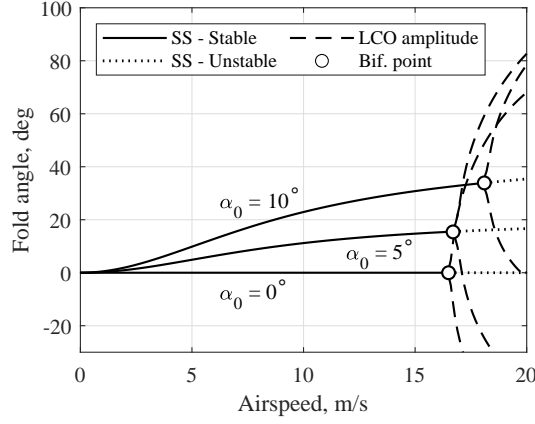


Fig. 17 Time response of an LCO at 17m/s at  $\alpha_0 = 0^\circ$



**Table 4 Comparison of the nonlinear and linear flutter speeds.**

Root angle of attack, $\alpha_0$ [°]	0	5	10
Nonlinear flutter speed [m/s]	16.5	16.7	18.2
Linear flutter speed [m/s]	16.6	17.2	19.8
Difference [%]	0.6	3.0	8.8



**Fig. 18 Bifurcation diagram of the fold angle representing the steady-state (SS) and LCO branches at root angles of attack,  $\alpha_0 = 0^\circ, 5^\circ$  and  $10^\circ$ .**

#### IV. Conclusions

This study has presented a low-fidelity nonlinear model to overcome the limitations, reported in previous work, of using linear models to represent the flared folding wingtip. The model divides the system into the main wing, represented as an Euler-Bernoulli beam, and the folding wingtip, represented as a rigid body. Next, the loads are introduced using a quasi-steady aerodynamic model that uses an exact representation of the geometrical angle of attack at the wingtip. Finally, the model is linearized and assembled into a state-space system later solved using the time-varying linear approximation method, a linear time domain solver that provides an instantaneous stability analysis as a by-product.

The model is validated using the experimental results from previous work. First, the results from a ground vibration test and the steady-state loads and deflections are used to update the structural and aerodynamic properties of the model that are later used in the time-marching solution. Following the model update, the natural frequencies of the wing are determined within a  $\pm 5\%$  difference with respect to the experimental values and the steady-state loads and deflections achieve good agreement of  $\pm 5\%$  with respect to those obtained in the wind tunnel.

The updated numerical model is used to assess the aeroelastic stability and dynamic response of the flared folding wingtip. First, the response to 1-cosine gusts of different frequencies is studied using the numerical model and compared to the experimental results. The model is found to provide a good agreement of the wing root bending moment load while exhibiting small differences in the time response of the fold angle. These differences are more prominent in the high-frequency gust of 8 Hz, corresponding to a reduced frequency of  $k = 0.220$ , which can be considered a highly unsteady case. In this case, small differences appear in the dynamic behavior of the system, which might be explained by the limitations of the aerodynamic model: in quasi-steady aerodynamics, there is no lag between the load and the response, contrary to what happens in unsteady aerodynamics.

Next, the flutter onset is studied at different root angles of attack,  $\alpha_0$ , for both free-hinge and locked-hinge conditions. On the one hand, in the free-hinge condition, the flutter onset is delayed when increasing  $\alpha_0$ , contrary to the results seen in the experiment, which was attributed to the inability of the numerical

model to account for the limits of the wind tunnel section in the out-of-plane direction. On the other hand, in the locked-hinge condition, increasing  $\alpha_0$  promotes flutter by reducing the frequency of the torsional mode, which is in agreement with other studies conducted in highly flexible wings.

The last comparison with the experiment addresses the gust load alleviation performance of the flared folding wingtip. On the one hand, the results show good agreement with the experiment, reproducing the peak load reduction and confirming the conclusions of previous studies: a late release of the wingtip can lead not only to increased peak loads but also to an increase in the oscillations of the system. On the other hand, the differences in the relative root mean square values, which increase with the gust frequency, show the limitations of the quasi-steady aerodynamic model. Ultimately, the model has shown its capability to reproduce the experimental results qualitatively, even though the quantitative agreement in the relative root mean square can still be improved.

Finally, the investigation of the limit cycle oscillations has shown that the post-flutter behavior is nonlinear, as observed in the experiment, leading to a set of limit cycle oscillations represented by a Hopf Bifurcation.

To conclude, future work on the model aims to improve the results presented in this study. First of all, the aerodynamic model will be updated to include unsteady aerodynamics to be able to better account for short, high-frequency gusts. Next, the setup of the initial experiment led to some uncertainties, such as the wing being partially submerged in the flow or the wind tunnel section being too small for large deflections. Therefore, a second experiment with the wing fully submerged in the flow is considered to improve the experimental results and reduce the uncertainties associated with the initial test. Finally, the increase of the oscillations due to the hinge release presents a motivation to include control surfaces on the model. First, such a numerical model would allow the study of possible synergies of conventional control surfaces and the flared folding wingtip to improve gust load alleviation. Next, a study could be conducted to find an adequate control law able to handle both the hinge release and the nonlinearities caused by the large deflections. Last, a new experiment can be designed to implement the control surfaces and the nonlinear control law and further validate the numerical model.

## References

- [1] Anderson, J. D., *Fundamentals of aerodynamics*, 6<sup>th</sup> ed., McGraw Hill, New York, 2017.
- [2] Smith, M. H., Renzelmann, M. E., and Marx, A. D., “Folding Wing-Tip System,” (U.S. Patent No. 5,381,986). U.S. Patent and Trademark Office, Jan. 17 1995. URL <https://worldwide.espacenet.com/patent/search?q=pn%3DUS5381986A>.
- [3] Wilson, T., Herring, M., Pattinson, J., Cooper, J., Castrichini, A., Ajaj, R., and Dhoru, H., “An Aircraft Wing With Moveable Wing Tip Device for Load Alleviation,” (International Patent No. WO2017/118832A1). World Intellectual Property Organization, Jul. 13 2017. URL <https://worldwide.espacenet.com/patent/search?q=pn%3DW02017118832A1>.
- [4] Castrichini, A., Siddaramaiah, V. H., Calderon, D., Cooper, J., Wilson, T., and Lemmens, Y., “Preliminary Investigation of Use of Flexible Folding Wing Tips for Static and Dynamic Load Alleviation,” *The Aeronautical Journal*, Vol. 121, No. 1235, 2017, p. 7394. <https://doi.org/10.1017/aer.2016.108>.
- [5] Cheung, R., Rezgui, D., Cooper, J., and Wilson, T., “Testing of a Hinged Wingtip Device for Gust Loads Alleviation,” *Journal of Aircraft*, Vol. 55, 2018, pp. 1–18. <https://doi.org/10.2514/1.C034811>.
- [6] Cheung, R., Rezgui, D., Cooper, J., and Wilson, T., “Testing of Folding Wingtip for Gust Load Alleviation of Flexible High-Aspect-Ratio Wing,” *Journal of Aircraft*, Vol. 57, No. 5, 2020, pp. 876–888. <https://doi.org/10.2514/1.C035732>.
- [7] Castrichini, A., Hodigere Siddaramaiah, V., Calderon, D., Cooper, J., Wilson, T., and Lemmens, Y., “Nonlinear Folding Wing Tips for Gust Loads Alleviation,” *Journal of Aircraft*, Vol. 53, No. 5, 2016, pp. 1391–1399. <https://doi.org/10.2514/1.C033474>.
- [8] Castrichini, A., Wilson, T., and Cooper, J., “On the Dynamic Release of the Semi Aeroelastic Wing-Tip Hinge Device,” *6th RAeS Aircraft Structural Design Conference*, 2018.

- [9] Dussart, G., Yusuf, S., and Lone, M., “Identification of In-Flight Wingtip Folding Effects on the Roll Characteristics of a Flexible Aircraft,” *Aerospace*, Vol. 6, 2019, p. 63. <https://doi.org/10.3390/aerospace6060063>.
- [10] Healy, F., Cheung, R., Neofet, T., Lowenberg, M., Rezgui, D., Cooper, J., Castrichini, A., and Wilson, T., “Folding Wingtips for Improved Roll Performance,” *AIAA Scitech 2021 Forum*, 2021. <https://doi.org/10.2514/6.2021-1153>.
- [11] Wilson, T., Kirk, J., Hobday, J., and Castrichini, A., “Small Scale Flying Demonstration of Semi Aeroelastic Hinged Wing Tips,” *18th International Forum on Aeroelasticity and Structural Dynamics (IFASD 2019)*, 2019.
- [12] Wilson, T., Kirk, J., Hobday, J., and Castrichini, A., “Update on AlbatrossONE Semi Aeroelastic Hinge Small Scale Flying Demonstrator Project,” *19th International Forum on Aeroelasticity and Structural Dynamics (IFASD 2022)*, 2022.
- [13] Carrillo, X., Mertens, C., Sciacchitano, A., van Oudheusden, B., Breuker, R. D., and Sodja, J., “Wing Stiffness and Hinge Release Threshold Effects on Folding Wingtip Gust Load Alleviation,” *AIAA Scitech 2022 Forum*, 2022. <https://doi.org/10.2514/6.2022-1559>.
- [14] Hodges, D. H., and Pierce, G. A., *Introduction to Structural Dynamics and Aeroelasticity*, 2<sup>nd</sup> ed., Cambridge University Press, 2011. <https://doi.org/10.1017/CBO9780511997112>.
- [15] Lago, A., Trabucco, D., and Wood, A., “Chapter 3 - Damping considerations in tall buildings,” *Damping Technologies for Tall Buildings*, Butterworth-Heinemann, 2019, pp. 39–106. <https://doi.org/10.1016/B978-0-12-815963-7.00003-8>.
- [16] Jrad, M., Zhao, W., Kapania, R. K., and Schmidt, D., “Elastic Axis Determination and Extraction of Vibration Mode Shapes of a Light Weight Composite Aircraft,” *AIAA Aviation Forum: Multidisciplinary Analysis and Optimization Conference*, 2018. <https://doi.org/10.2514/6.2018-3429>.
- [17] Elsayed, M. S. A., Sedaghati, R., and Abdo, M., “Accurate Stick Model Development for Static Analysis of Complex Aircraft Wing-Box Structures,” *AIAA Journal*, Vol. 47, 2009, pp. 2063–2075. <https://doi.org/10.2514/1.38447>.
- [18] Healy, F., Cheung, R. C., Rezgui, D., and Cooper, J. E., “Nonlinear Stability Analysis and Experimental Exploration of Limit Cycle Oscillations with Flared Folding Wingtips,” *AIAA Scitech 2022 Forum*, 2022. <https://doi.org/10.2514/6.2022-0657>.
- [19] Dimitriadis, G., *Introduction to Nonlinear Aeroelasticity*, Wiley, 2017. <https://doi.org/10.1002/9781118756478>.
- [20] Healy, F., Cheung, R. C., Rezgui, D., Cooper, J. E., Wilson, T., and Castrichini, A., “On the Nonlinear Geometric Behaviour of Flared Folding Wingtips,” *AIAA Scitech 2022 Forum*, 2022. <https://doi.org/10.2514/6.2022-0656>.
- [21] Tang, D. M., and Dowell, E. H., “Effects of geometric structural nonlinearity on flutter and limit cycle oscillations of high-aspect-ratio wings,” *Journal of Fluids and Structures*, Vol. 19, 2004, pp. 291–306. <https://doi.org/10.1016/j.jfluidstructs.2003.10.007>.
- [22] Drachinsky, A., Avin, O., Raveh, D. E., Ben-Shmuel, Y., and Tur, M., “Flutter Tests of the Pazy Wing,” *AIAA Scitech 2022 Forum*, 2022. <https://doi.org/10.2514/6.2022-2186>.
- [23] Geertsen, J., “Development of a Gust Generator for a Low Speed Wind Tunnel,” ETH Zürich, 2020. (Unpublished master’s thesis).